ACS APPLIED MATERIALS & INTERFACES

www.acsami.org

Research Article

The High Anisotropy of the Epitaxial Growth of the Well-Aligned Sb_2Se_3 Nanoribbons on Mica

Jinyang Liu,* Mingling Li, Mengyu Liu, Hongbing Cai,* Yue Lin,* Yuhan Zhou, Zhigao Huang, and Fachun Lai

Cite This: *ACS Appl. Mater. Interfaces* 2020, 12, 9909–9917

Read Online

ACCESS | Metrics & More | Article Recommendations | Supporting Information

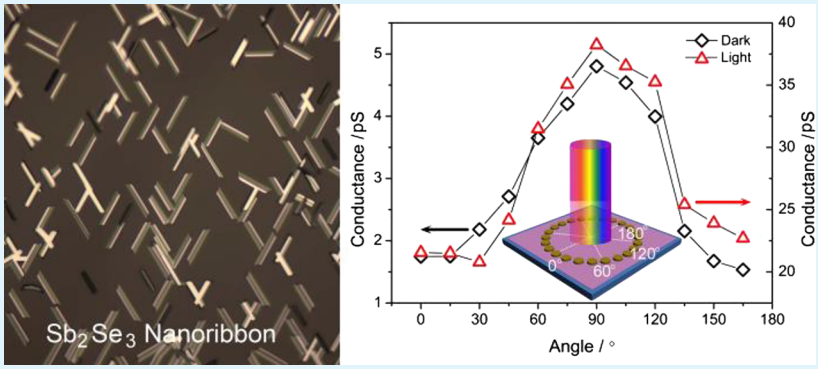

ABSTRACT: One-dimensional semiconductor nanostructures, which are different from those of bulk materials, have attracted considerable interest in either scientific research or practical application. Herein, the Sb_2Se_3 nanoribbons have been successfully synthesized by the epitaxial growth process on mica using the rapid physical vapor deposition method. The density of the Sb_2Se_3 nanoribbons increased quickly when the temperature decreased, and finally, the nanoribbons connected to each other and formed a network structure even in film. These nanoribbons were all well aligned along the preferred direction that either is parallel to each other or forms 60° angles. Further structural investigation demonstrated that the Sb_2Se_3 nanoribbons grew along the [001] directions, which are aligned along the directions [1$\bar{1}$0] and [100] or [100] and [110] on the mica surface. Then, an asymmetric lattice mismatch growth mechanism causing incommensurate heteroepitaxial lattice match between the Sb_2Se_3 and mica crystal structure was suggested. Furthermore, a polarized photodetector based on the film with the well-aligned Sb_2Se_3 nanoribbons was constructed, which illustrated strong photosensitivity and high anisotropic in-plane transport either in the dark or under light. The incommensurate heteroepitaxial growth method shown here may provide access to realize well-ordered nanostructures of other inorganic materials and promote the anisotropic photodetector industrialization.

KEYWORDS: *Sb_2Se_3 nanoribbons, rapid physical vapor deposition, anisotropic photodetectors, heteroepitaxial growth, well-aligned*

INTRODUCTION

In the past few years, one-dimensional (1D) semiconductors, especially the nanotubes, nanowires, and nanoribbons, have gained plenty of attention owing to their excellent optical, electrical, catalytic, and mechanical properties.[1,2] On account of their prospective applications in thermoelectric devices, optoelectronic devices, and solar cells, the main-group metal chalcogenides such as V−VI (V = As, Sb, Bi; VI = S, Se, Te) group compounds have received a great deal of attention.[3,4] Among these semiconductors, Sb_2Se_3, a direct and narrow bandgap p-type semiconductor (~1.21 eV), has wide applications in electric, photoelectric, photovoltaic, and electrochemical devices attributed to its high environmental stability, Seebeck coefficient, and thermoelectric power,[5,6] as well as the excellent photovoltaic properties. Many efforts have been made to synthesize Sb_2Se_3 nanostructures inspired by their excellent characteristics in recent years. The chemical bottom-up process is suggested to be a favorable method in practical applications.[7−9] Actually, lots of Sb_2Se_3 nanostructures, including nanowires,[7] nanorods,[9] nanoneedles,[8] nanoribbons,[10] and nanosheets,[11] have been synthesized by solution methods. However, the capping ligands that remained on the nanostructure surface usually become a disadvantage for further application. Therefore, the physical method is regarded as a much more efficient method for fabricating nanomaterials.[12,13] In fact, large quantities of Sb_2Se_3 nanostructures

Received: November 6, 2019
Accepted: February 3, 2020
Published: February 3, 2020

https://dx.doi.org/10.1021/acsami.9b20142
ACS Appl. Mater. Interfaces 2020, 12, 9909−9917

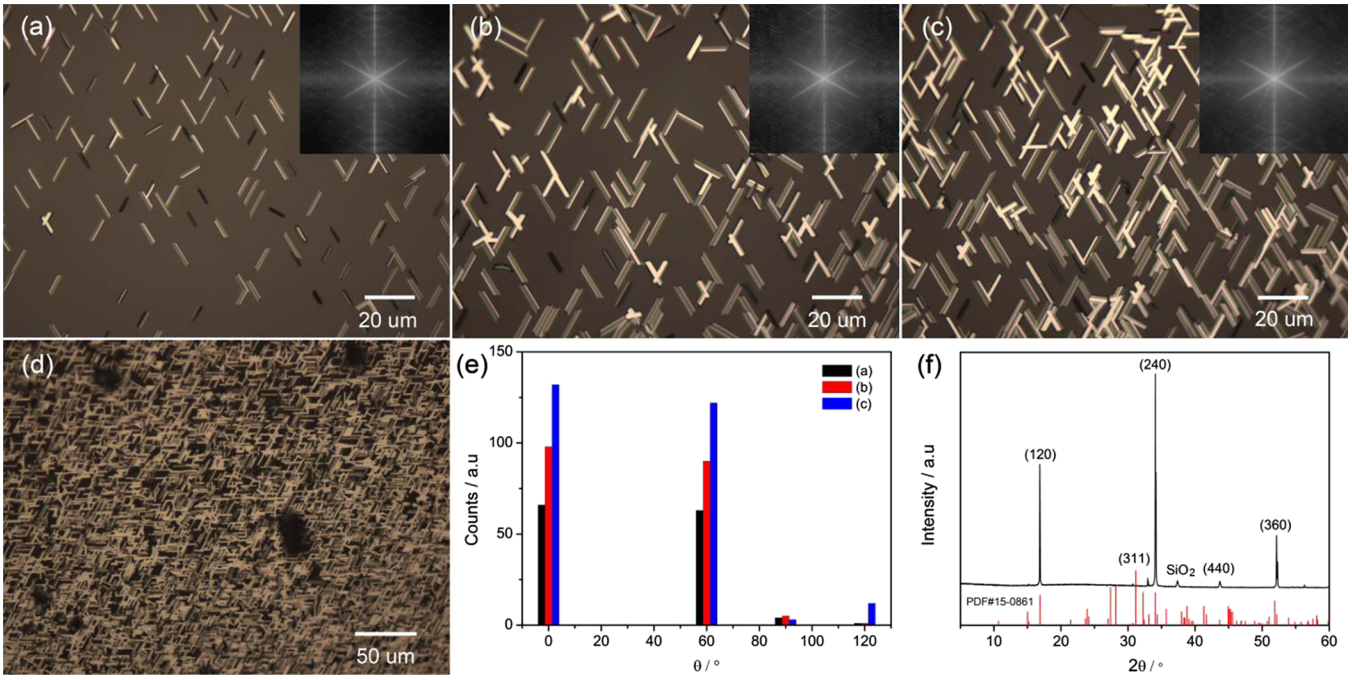

Figure 1. Morphology and phase structure of the well-aligned Sb_2Se_3 nanoribbons. (a–d) OM images of the Sb_2Se_3 nanoribbons epitaxially grown on the mica substrate from high to low temperatures. (e) Statistical data of the intersection angle between the Sb_2Se_3 nanoribbons illustrated in (a)–(c). (f) XRD pattern of the well-aligned Sb_2Se_3 nanoribbons transferred on SiO_2.

applied in the solar cell using the physical vapor deposition (PVD) method have been systematically investigated. For example, one-dimensional well-aligned Sb_2Se_3 ribbons with benign grain boundaries were reported to form thin-film photovoltaics using the rapid thermal evaporation (RTE) method.[13] The Sb_2Se_3 thin-film solar cell with 7.6% efficiency was obtained by a vapor transport deposition (VTD) process.[3] Recently, the Sb_2Se_3 nanorod arrays have been synthesized by the close-spaced sublimation (CSS) method, and a certified efficiency of 9.2% of the solar cell was achieved.[6] However, most research studies on Sb_2Se_3 by the PVD method are focused on the 2D materials (thin film),[14,15] and the 1D nanostructure is rarely investigated. Furthermore, in Sb_2Se_3, $(Sb_4Se_6)_n$ ribbons stack along the [001] direction through strong covalent Sb–Se bonds, whereas in the [100] and [010] directions, the $(Sb_4Se_6)_n$ ribbons are held together by van der Waals (vdW) forces.[13] Consequently, Sb_2Se_3 tends to form a 1D nanostructure along the [001] direction due to its unique crystal structure.[7,13] In addition, the carrier prefers to transport in the [001] direction rather than other directions. The devices constructed with this unique orientation are expected to offer appealing anisotropic photoresponse.[5,13] However, as far as we know, a little is studied about 1D Sb_2Se_3 nanostructures synthesized by the vapor deposition method.[16–18]

Herein, 1D Sb_2Se_3 nanoribbons have been synthesized by the rapid physical vapor deposition (rPVD) technique. The nanoribbons were all horizontally bound on mica, well aligned with preferred orientations that either are parallel to each other or form 60° angles. These Sb_2Se_3 nanoribbons epitaxially grow along [001], oriented preferentially parallel to two of three high symmetry crystallographic directions of mica [100] and [110] or [100] and [1$\bar{1}$0] and finally forming 60° angles after systematical morphology and structure characterization and analysis. Then, an asymmetric lattice mismatch growth mechanism causing an incommensurate heteroepitaxial lattice match between Sb_2Se_3 and the mica substrate was proposed. In addition, a photodetector based on the film with the well-aligned Sb_2Se_3 nanoribbons was constructed, and the device illustrated strong photosensitivity and high anisotropic in-plane transport either in the dark or under light. The work illustrated here may provide great potential guidance for synthesizing well-ordered nanostructures using the incommensurate epitaxial growth method and advance the progress of the anisotropic photodetectors.

RESULTS AND DISCUSSION

The well-aligned Sb_2Se_3 nanoribbons were synthesized by the rPVD technique explored in our group.[19] Figure 1 describes typical optical microscopy (OM) images of the as-product. The nanoribbons are grown on the mica downstream from high to low temperatures. It can be seen that lots of the Sb_2Se_3 nanoribbons were horizontally bound on the mica (001) surface. The density of the Sb_2Se_3 nanoribbons was very low in the high temperature, as shown in Figure 1a, while the density increased quickly as the temperature decreased, and finally, the nanoribbons connected to each other and formed the network structure (shown in Figure 1d) even the film (as shown in Figure S1). Such density difference in positions could be contributed to the temperature and source gradient on the substrate surface. More interestingly, these Sb_2Se_3 nanoribbons are well aligned, which either are parallel to each other or form 60° angles with very little mismatched. To further study the orientation of these nanoribbons, the intersection angles between the Sb_2Se_3 nanoribbons in Figure 1a–c were carefully counted, and the corresponding data are illustrated in Figure 1e. The results showed that most of the Sb_2Se_3 nanoribbons exhibited intersection angles of 60°, and only a few nanoribbons had intersection angles of 120° or 90°. In addition, to further characterize the orientation of these nanoribbons, 2D fast Fourier transform (FFT) (characterized

https://dx.doi.org/10.1021/acsami.9b20142
ACS Appl. Mater. Interfaces 2020, 12, 9909–9917

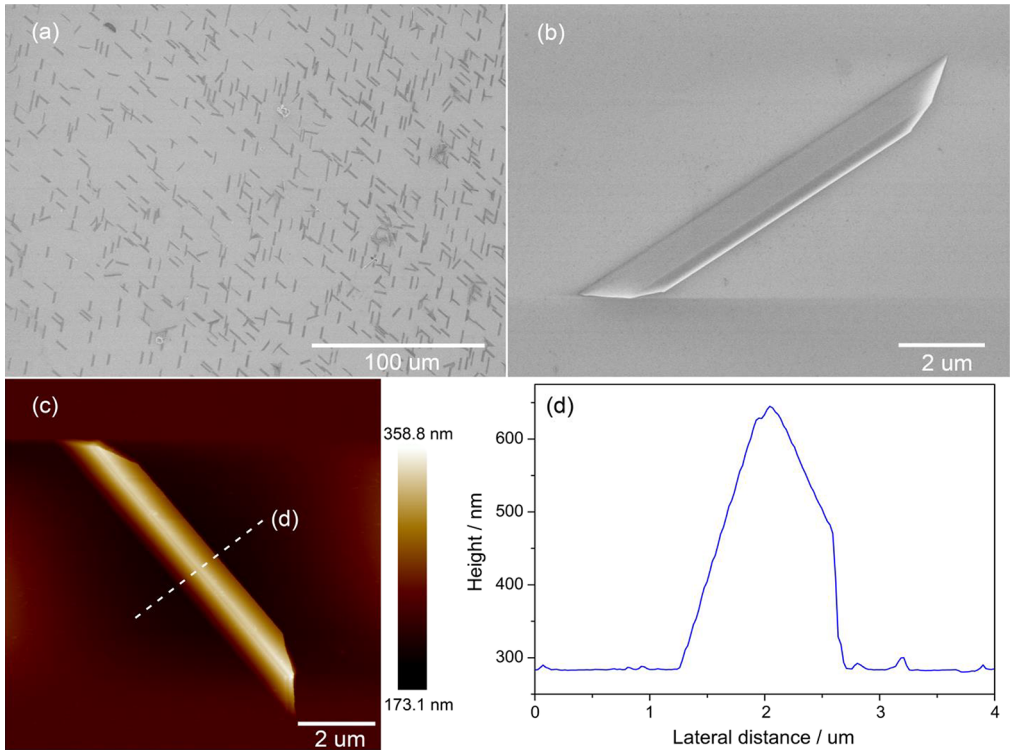

Figure 2. SEM and AFM characterization of the well-aligned Sb_2Se_3 nanoribbons. (a, b) SEM image with low and high magnifications of the Sb_2Se_3 nanoribbons transferred onto SiO_2/Si substrate, respectively. (c) AFM image of the Sb_2Se_3 nanoribbons. (d) Corresponding section line shown in (c).

using ImageJ software) on the optical images was performed, and the results are described in the upper right inset in Figure 1a–c, which shows six streaks evenly spread every 60°. An important point that should be noticed is the unique growth directions of these nanoribbons, and these are suggested to be independent of the thermal evaporation temperatures after a series of experiments with different thermal evaporation temperatures (as shown in Figure S2). It agrees with the 6-fold symmetrical properties of the mica (001) surface. This may be caused by the epitaxial growth, and extensive and in-depth discussion will be made later.

The phase structure of the well-aligned Sb_2Se_3 nanoribbons was investigated by powder X-ray diffraction (XRD) analysis. The results are demonstrated in Figure 1f (well-aligned Sb_2Se_3 nanoribbons transferred to the SiO_2 substrate). All the peaks are consistent with the orthorhombic phase of Sb_2Se_3 (PDF #15-0861, a = 11.63 Å, b = 11.78 Å, c = 3.985 Å). No peaks of any other phases except SiO_2 are detected. This indicates that the as-prepared Sb_2Se_3 nanoribbons are high-purity, single-phase nanostructures. The dominant XRD peaks are located at 16.89°, 34.03°, and 52.09°, which corresponds to lattice planes (120), (240), and (360). It should be pointed out that only signals from {120} could be found in the XRD pattern, while those from the {001} plane are systematically absent. It could be concluded that the nanoribbons have a preferred growth direction of [001].[20] This agrees with the fact that the as-products have a ribbon-like morphology due to their unique crystal structure, as illustrated in Figure S3.

To further study them, the Sb_2Se_3 nanoribbons were transferred onto the SiO_2/Si substrate for scanning electron microscopy (SEM) characteristics. The result is illustrated in Figure 2a,b. The Sb_2Se_3 nanoribbons look very smooth and clean with a width of ~1 μm and a length of ~10 μm. In addition, these nanoribbons were all well aligned, either parallel to each other or forming 60° angles, indicating the high transferred quality. To measure the thickness of the as-products, atomic force microscopy (AFM) was used. The results described in Figure 2c,d shows that the maximum thickness was measured to be ~360.0 nm according to the cross-section line shown in Figure 2d. Extensive SEM and AFM characterizations indicate that the nanoribbons have average sizes of 8–10 μm in length, 950–1100 nm in width, and 345–360 nm in thickness. The width of the Sb_2Se_3 nanoribbons was about three times larger than the thickness, and the typically actual cross-section is shown in Figure S4. In addition, Raman spectra revealed a lot of information about the crystal orientation and quality of the nanomaterials. From Figure S5, Raman peaks at 189.6 and 252.9 cm^{-1} were clearly observed. As previously reported,[11] the peak at 185 cm^{-1} corresponds to A_g mode, while the peak at 250 cm^{-1} corresponds to B_{1g} mode. Therefore, Raman shift values of 4.6 cm^{-1} for A_g and 2.9 cm^{-1} for A_g were observed. Such a blue shift may be caused by the weaker long-range Coulombic interaction in thinner samples.[11,21,22] In addition, all Raman peaks agree well with the previously reported results,[11] indicating that the Sb_2Se_3 nanoribbons synthesized here have a high quality. The absorption coefficient demonstrated the slow increase from 1.0 to 1.2 eV and rapid increase at ~1.2 eV, and further study indicated that it is an indirect bandgap with 1.2 eV (as shown in Figure S6). Furthermore, the room-temperature photoluminescence (PL) properties of the as-prepared Sb_2Se_3 nanoribbons have been investigated, and a strong PL peak at ~942 nm ($E_g \approx 1.31$ eV) was observed (shown in Figure S7), gaining a great interest in near-infrared-based optoelectronic devices.

https://dx.doi.org/10.1021/acsami.9b20142
ACS Appl. Mater. Interfaces 2020, 12, 9909–9917

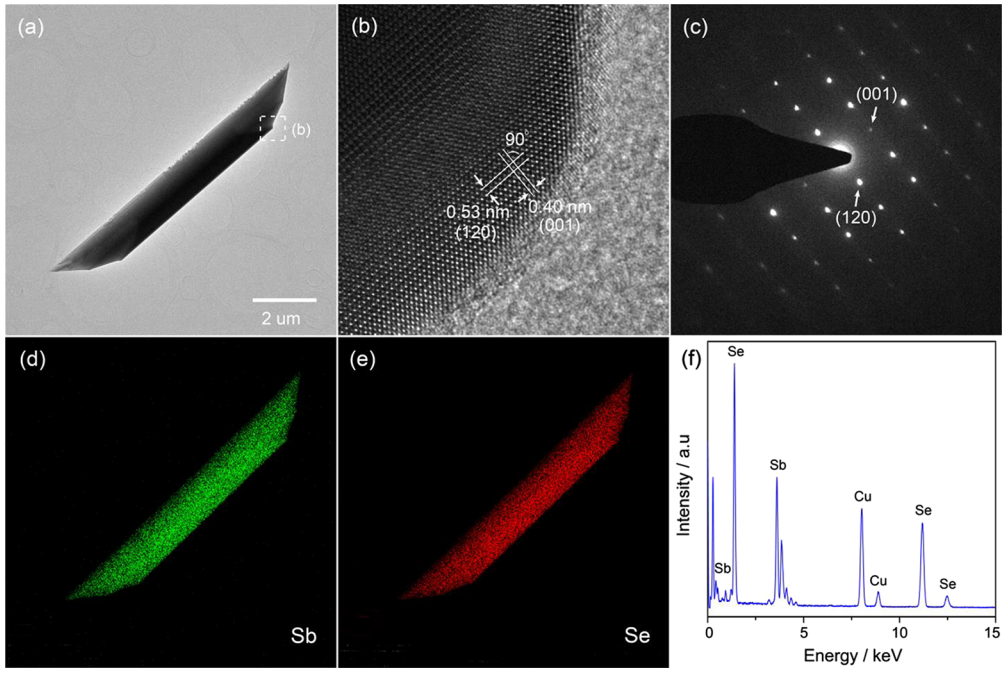

Figure 3. Microstructure and chemical composition characterization. (a) TEM image of the representative Sb_2Se_3 nanoribbons. (b) HR-TEM image of the selected area in representative Sb_2Se_3 nanoribbons of (a). (c) SAED pattern of the Sb_2Se_3 nanoribbons. (d, e) Sb and Se element mapping of the same Sb_2Se_3 nanoribbon, respectively. (f) EDX spectrum of the Sb_2Se_3 nanoribbons.

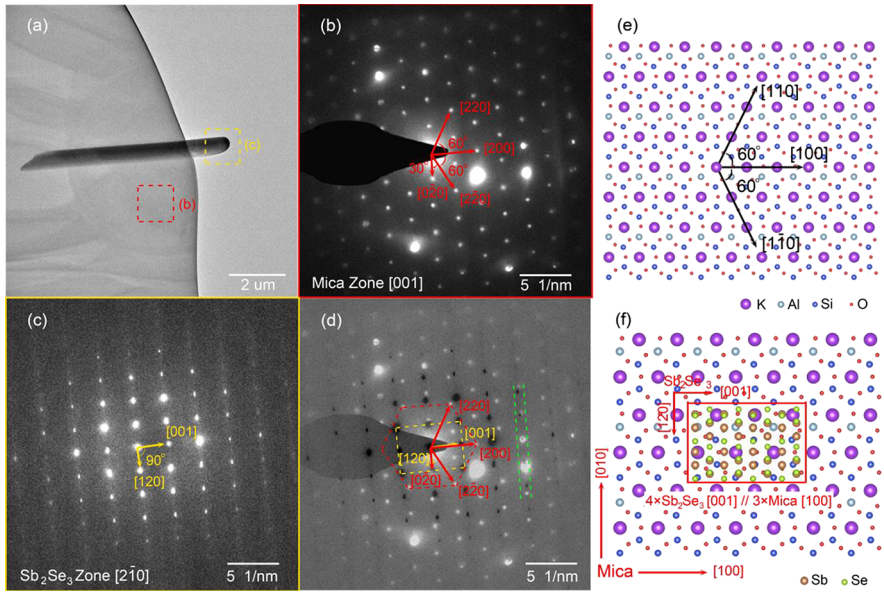

Figure 4. In situ SAED pattern of the mica and Sb_2Se_3 nanoribbons. (a) TEM image of the suspended Sb_2Se_3 nanoribbons on the mica edge. (b, c) SAED pattern of the mica substrate and suspended Sb_2Se_3 nanoribbons indicated in region 1, respectively. (d) Combined SAED pattern of the Sb_2Se_3 nanoribbons (black dots) and mica (white dots) shown in (b) and (c). (e) Atomic structure of mica substrate and (f) schematics of the atomic arrangement of the Sb_2Se_3 structure on the (001) plane of the mica surface. The red square indicated a proposed incommensurate heteroepitaxial relationship.

The crystal structure of as-prepared Sb_2Se_3 nanoribbons was characterized by high-resolution transmission electron microscopy (HR-TEM) and selected-area electron diffraction (SAED), and chemical composition was further evaluated by energy-dispersive X-ray (EDX) spectroscopy. The representative bright TEM image illustrated in Figure 3a clearly indicates the nanoribbon-like structure. The HR-TEM image (Figure 3b) of the marked square in Figure 3a exhibits lattice spacing values of ~0.40 and 0.53 nm, which belong to the (001) and (120) plane spacing of orthorhombic phase Sb_2Se_3, respectively. In addition, an angle of 90° is observed between (001) and (120) planes. The SAED pattern taken from an individual nanoribbon (Figure 3c) confirms that the product is a single crystal grown along the [001] direction, which is consistent with the HR-TEM image (Figure 3) and XRD spectrum (Figure 1f) shown above. The chemical composition of the individual Sb_2Se_3 nanoribbon was further investigated using the EDX spectroscopy. As illustrated in Figure 3d,e, EDX

https://dx.doi.org/10.1021/acsami.9b20142
ACS Appl. Mater. Interfaces 2020, 12, 9909−9917

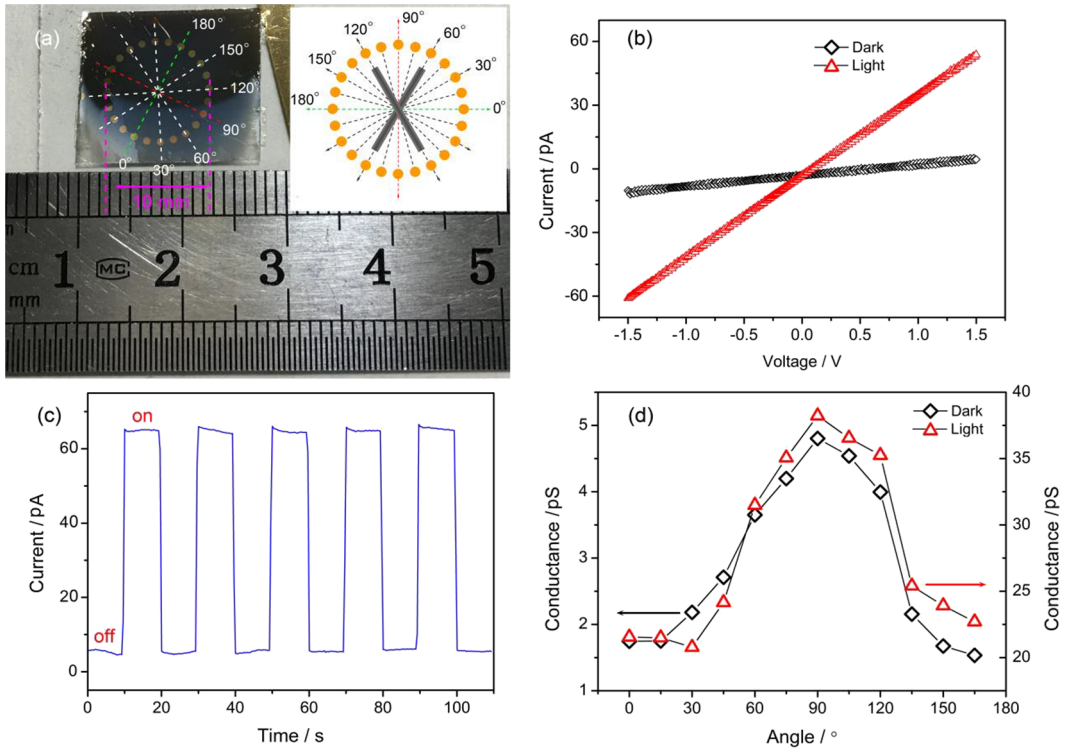

Figure 5. In-plane anisotropy photoresponse of the device fabricated with the film composed of well-aligned Sb_2Se_3 nanoribbons. (a) Photography of the device based on the film with the well-aligned Sb_2Se_3 nanoribbons and inset showing the schematic setup for the angle-resolved $I-V$ measurement. (b) Typical $I-V$ curves of this photodetector in the dark and under white light. (c) Photoresponse of the device at 1.5 V with and without white light. (d) Angle-dependent conductivity of the device under white light or not.

element mapping images confirm the uniform chemical distribution in the whole nanoribbon. In addition, the corresponding EDX spectrum (Figure 3f) exhibits a Sb/Se atomic ratio of ~1:1.51, further indicating that the product is the Sb_2Se_3 nanoribbon. Therefore, it can be concluded that the as-products are the Sb_2Se_3 nanoribbons grown along the [001] direction, with the $(2\bar{1}0)$ plane parallel to the mica substrate.

How does the unique orientation of the Sb_2Se_3 nanoribbons grown on the mica surface occur? As is well known to all, the mica substrate is composed of layered structures, and a freshly cleaved mica surface is expected to be atomically smooth and free of dangling bonds.[20,23] In detail, each fresh cleavage mica has the same (001) crystal plane, and the surface is arranged with two of the three high-symmetry directions $[1\bar{1}0]$ and [100] or [100] and [110], which leads to the formation of a 2-fold symmetry surface construct separated by a cleavage step.[23,24] Further, an angle of 60° between the high-symmetry directions appeared in both cases, as shown in Figure 4e.[23] On the strength of the preferred angle of 60° between the Sb_2Se_3 nanoribbons and the high-symmetrical property of the (001) plane of the mica surface, it can be considered that the nanoribbons are aligned along the directions $[1\bar{1}0]$ and [100] or [100] and [110] on the mica cleavage plane depending on its surface arrangement. Therefore, to further understand their unique orientation relationship, the in situ SAED patterns of the suspended Sb_2Se_3 nanoribbons and the mica substrate were adopted. As shown in the low-magnification TEM image illustrated in Figure 4a, a suspended Sb_2Se_3 nanoribbon was clearly observed on the ultrathin mica edge. Figure 4b demonstrates the typical SAED patterns of the ultrathin mica substrate around the suspended Sb_2Se_3 nanoribbon shown in Figure 4a. The results illustrated that the mica was a single crystal with patterns distributed in 6-fold symmetry, which was consistent with previous reports.[25,26] In addition, the SAED patterns of the suspended Sb_2Se_3 nanoribbon indicated that it was a single crystal grown along the [001] direction, which was consistent with the transferred Sb_2Se_3 nanoribbon characterized by HR-TEM (Figure 3b), SAED (Figure 3c), and XRD (Figure 1f). Then, the SAED patterns of the suspended Sb_2Se_3 nanoribbons and the mica substrate were combined together, as demonstrated in Figure 4d. The black dots are the SAED pattern of the mica, while the white dots belong to the SAED pattern of Sb_2Se_3. The results suggested that the Sb_2Se_3 nanoribbons in the [001] direction grew along the [100] direction of the mica substrate, while Sb_2Se_3 nanoribbons in the [120] direction were located along the $[0\bar{1}0]$ direction of the mica, namely, $Sb_2Se_3[001]\|$mica [100] and $Sb_2Se_3[120]\|$mica $[0\bar{1}0]$. However, the 1.8° offset between these two directions was observed. This may come from the different lattice types of these materials and the orientation optimization to maximize the vdW bonding.[27] Furthermore, the electron diffraction point of Sb_2Se_3 (003) nearly coincided with the electron diffraction point of mica (400), indicating that there is a minimum lattice mismatch between the Sb_2Se_3 (001) and mica (100) with $4d_{Sb2Se3(001)} \approx 3d_{mica(100)}$. The lattice d-spacing values of Sb_2Se_3(001) and (120) are 3.985 and 5.250 Å, respectively (PDF#15-0861). The values of mica (100) and (010) are 5.19 and 9.03 Å, respectively (PDF#06-0623). The mismatch between Sb_2Se_3 and mica $f = (1 - d_{overlayer}/d_{substrate}) \times 100\%$ is estimated to be ~41.8%, while the lattice mismatch between the Sb_2Se_3 (001) and mica (100) with $4d_{Sb2Se3(001)} \approx 3d_{mica(100)}$ is as low as 2.37%. In addition, the lattice mismatch between the Sb_2Se_3 (120) and mica $(0\bar{1}0)$ was very large, up to 41.8%, while the lattice mismatch with

https://dx.doi.org/10.1021/acsami.9b20142
ACS Appl. Mater. Interfaces 2020, 12, 9909−9917

$12d_{Sb2Se3(120)} \approx 7d_{mica(0\text{-}10)}$ is as low as 0.33%. All in all, the Sb_2Se_3 lattice mismatch between the Sb_2Se_3 (001) and mica (100) is much smaller than that between the Sb_2Se_3 (120) and mica ($0\bar{1}0$), which resulted in the unlimited growth of Sb_2Se_3 in the [001] direction while restricting the width of Sb_2Se_3 in the [120] direction on the mica surface, finally resulting in the formation of a 1D nanoribbon.[28] Furthermore, the top view of the atomic arrangement between the Sb_2Se_3 nanoribbon and the (001) plane of the mica surface is proposed and shown in Figure 4f. As is known to all, the incommensurate vdW force affords almost all lattice relaxation between the layered as-products and the mica substrate,[26,29] and it can be concluded that the Sb_2Se_3 nanoribbons exhibit incommensurate epitaxial growth on the mica surface.

To investigate their strong in-plane anisotropy and the unique well-aligned structure of the Sb_2Se_3 nanoribbons in application, the photodetectors based on the film with the well-aligned Sb_2Se_3 nanoribbons shown in Figure 1d were fabricated (device fabrication details illustrated in Experimental Section). As shown in Figure 5a, 24 electrodes (10 nm Ti/100 nm Au) in a spherical manner (10 mm in diameter) with an interelectrode angle of 15° were deposited onto the Sb_2Se_3 film, and two couple electrodes were oriented parallel to the Sb_2Se_3 nanoribbons, as illustrated in the schematic diagram in the right inset. The angle between the diagonal bisector of 120° of the Sb_2Se_3 nanoribbons is defined as the intersection angle, and consequently, the electrode angle between the diagonal bisector of 60° of the Sb_2Se_3 nanoribbons is 90°, as demonstrated in the schematic diagram (the right corner in Figure 5a). The measured $I-V$ curves of this device (the electrodes in 90°) are nearly linear, as illustrated in Figure 5b, indicating an ohmic contact. Furthermore, the electronic current increased remarkably at white light illumination in contrast to the dark due to the fact that light illumination can excite electron−hole pairs, resulting in an increase in conductance. The photocurrent measured at 1.5 V indicated that the device is a well-performing white light photodetector (Figure 5c). First, the reversibility and stability indicate that it a robust device, which is much better than that constructed with Sb_2Se_3 nanoribbons synthesized by the solution approaches (as shown in Figure S8). Second, the photoresponse I_{on}/I_{off} defined as the ratio of the current under white light to dark could reach as high as ∼1096%, as large as one order of magnitude. Third, the response time is very short. It is within 0.8 s, and the recovery time can be less than 0.8 s, as shown in Figure S9, in our device. In addition, strong angle-dependent conductivity was observed: in the dark, the conductivity increases from 0° to 90° and then decreases from 90° to 180°; a maximum conductivity of 4.8 nS in 90° and a minimum conductivity of 1.5 nS in 0° were observed (Figure 5d), leading to a $\sigma_{max}/\sigma_{min}$ ratio of 3.2. Under white light, the evolution between the conductivity and the angle well agreed with that in the dark; a maximum conductivity of 38.2 nS in 90° and a minimum current of 20.8 nS in 0° were observed (Figure 5d), which are much larger than those in the dark, indicating high photosensitivity in different angles. As is known to all, the hole mobility in polycrystalline Sb_2Se_3 is different in different crystal directions, which indicated high anisotropy.[5] The conductivity anisotropy may be ascribed to two factors: one is the anisotropic mobility within the Sb_2Se_3 nanoribbons, and another is the unique orientation of Sb_2Se_3 nanoribbons. However, on further analysis, it is found that the maximum conductivity is located at the 90° electrode, which is the diagonal bisector of 60°, and the minimum conductivity is positioned at the 0° electrode, which is the diagonal bisector of 120° either in the dark or under light. Therefore, it can be concluded that the strong photosensitivity and high anisotropic in-plane transport of the photodetector constructed with the film with the well-aligned Sb_2Se_3 nanoribbons originated from the unique orientation of Sb_2Se_3 nanoribbons and its intrinsic anisotropic property. Furthermore, the anisotropic photodetectors based on different 2D materials have been compared, and the results are shown in Table S1. It can be seen that our device contained the higher anisotropic in-plane transport ($\sigma_{max}/\sigma_{min}$) compared with the photodetector-based TiS_3 nanosheet,[30] BP sheet,[31] GeSe nanosheet,[32] and GeP flake.[33] Although the $\sigma_{max}/\sigma_{min}$ in our device is lower than that in the Sb_2Se_3 nanosheet,[11] the size in our device (10 mm in diameter) is much larger, and it may have a much practical application.

CONCLUSIONS

The well-aligned Sb_2Se_3 nanoribbons have been successfully synthesized by the epitaxial growth process on mica using the rPVD method. The density of the Sb_2Se_3 nanoribbons increased quickly from high to low temperatures and finally connected each other and formed the network structure even the film. These nanoribbons were all horizontally bound on mica, well-aligned with a preferred direction that either is parallel to each other or forms 60° angles. Structural characterization indicated that mica and Sb_2Se_3 may have an asymmetric lattice match along with different crystallographic directions and cause the incommensurate heteroepitaxial growth. Furthermore, a photodetector based on the film with the well-aligned Sb_2Se_3 nanoribbons was fabricated, and the device illustrated strong photosensitivity and high anisotropic in-plane transport either in the dark or under light after systematical analysis. This work shown here may provide useful insight into a deep understanding of the epitaxial growth method in synthesizing well-ordered nanostructures and provide access for the application in anisotropic photodetectors.

EXPERIMENTAL SECTION

Synthesis Process. The well-aligned 1D Sb_2Se_3 nanoribbons are synthesized using the rPVD method.[19] Typically, the quartz boat containing 0.05 g of Sb_2Se_3 powder (Jiangxi Ketai Advanced Materials Co. Ltd., 99%) was used as the source and placed in the center. The freshly cleaved mica (∼1 × 4 cm) was put downstream from the center (∼18−22 cm). The quartz tube was first pumped to ∼10 Pa and cleaned with ultrapure Ar. Then, after reaching the target temperature of 550 °C in 25 min with 30 sccm Ar, the quartz boat with Sb_2Se_3 powder was inserted into the heating zone and sustained for 7 min with 30 sccm Ar and 3 sccm H_2. At the moment, the temperature of the heating zone was 550 °C, while the temperature of the mica substrate was 341−459 °C. It should be noted that the quartz boat with the Sb_2Se_3 powder should be away from the heating center in the heating process. At last, quick cooling down of the furnace was applied through opening the stove.

Transfer Method. The well-aligned Sb_2Se_3 nanoribbons were transferred from the mica to the SiO_2/Si substrate by a water ultrasonic method.[34] In a typical transfer process, the mica with Sb_2Se_3 nanoribbons was spin-coated with poly(methyl methacrylate) (PMMA; A4 495K, MicroChem) at 2000 rpm for 45 s and heated at 120 °C for 3 min. The whole sample was floated on the water and separated through ultrasonication for several hours. After that, PMMA containing nanoribbons was rinsed and transferred to a silica substrate and copper grid (TEM test). After drying for several hours at room

https://dx.doi.org/10.1021/acsami.9b20142
ACS Appl. Mater. Interfaces 2020, 12, 9909−9917

temperature, the PMMA was removed by acetone. To in situ-characterize the SAED patterns, the thickness of the mica substrate grown with the well-aligned Sb_2Se_3 nanoribbons was carefully reduced using the in situ mechanical exfoliation , and then immobilized with a twin copper ring gauge.

Device Fabrication. The photodetectors based on the film with the well-aligned Sb_2Se_3 nanoribbons were fabricated using a hard template. First, a photomask containing 24 electrodes arranged in a circle with interelectrode angles of 15° and 10 mm in couple electrodes was designed and fabricated by maskless lithography. Two couple electrodes in the photomask were parallel to the two preferred directions of the Sb_2Se_3 nanoribbons and then immobilized above the mica substrate with as-products under optical microscopy with a rotating platform. The 10/100 nm Ti/Au was deposited by sputtering used as electrodes, and the devices were constructed finally by tearing the photomask. Therefore, two couple electrodes were parallel to two preferred directions of the Sb_2Se_3 nanoribbons with angles of 60° or 120°, and the schematic to fabricate the device is exhibited in Figure S10.

Characterization. The morphologies and distribution of Sb_2Se_3 nanoribbons were characterized by optical microscopy (OM) (Olympus BX51M) and scanning electron microscopy (SEM) (Hitachi SU-8010). The phase structure, height, and width of the Sb_2Se_3 nanoribbons were characterized by powder X-ray diffraction (XRD) pattern (Cu Kα, λ = 0.15418 nm) and atomic force microscopy (AFM) (Bruker Dimension Icon), respectively. Transmission electron microscopy (TEM), high-resolution TEM (HR-TEM), energy-dispersive X-ray spectroscopy (EDX), and selected-area electron diffraction (SAED) patterns were collected by an FEI Talos transmission electron microscope operated at 200 kV. The Raman spectroscopy was recorded by HORIBA Jobin Yvon Evolution (532 nm, 5 mW). The photomask containing 24 electrodes in a circle with interelectrode angles of 15° was designed and fabricated by maskless lithography (ATD1500, Advantools (China) Co., Ltd.). The Ti/Au(10/100 nm) electrodes were fabricated by sputtering (Sputter-Lesker Lab18). The electronic properties were characterized using a semiconductor parameter analyzer (Keithley, 4200-SCS). A tungsten lamp (OPTEM) was used as a source of white light (2.65 mW cm^{-2}).

■ ASSOCIATED CONTENT

Supporting Information

The Supporting Information is available free of charge at https://pubs.acs.org/doi/10.1021/acsami.9b20142.

Morphology of the film, OM images of the Sb_2Se_3 nanoribbons epitaxially grown with different thermal evaporation temperatures, schematic of the crystal structure, cross-sectional view of the Sb_2Se_3 nanoribbon, absorption and PL spectrum, photoresponse of the photodetector constructed with solution-processed Sb_2Se_3 nanoribbons, photocurrent rise and decay of the photodetector device, and schematic of the device fabrication process (PDF)

■ AUTHOR INFORMATION

Corresponding Authors

Jinyang Liu − *College of Physics and Energy, Fujian Normal University, Fuzhou 350117, P. R. China; Fujian Provincial Key Laboratory of Quantum Manipulation and New Energy Materials, Fuzhou 350117, P. R. China; Fujian Provincial Collaborative Innovation Center for Optoelectronic Semiconductors and Efficient Devices, Xiamen 361005, P. R. China; Fujian Provincial Engineering Technology Research Center of Solar Energy Conversion and Energy Storage, Fuzhou 350117, China;* orcid.org/0000-0001-8883-4656; Phone: +86-18120795008; Email: jyliu@fjnu.edu.cn

Hongbing Cai − *Hefei National Laboratory for Physical Science at the Microscale, University of Science and Technology of China, Hefei 230026, Anhui, P. R. China; Division of Physics and Applied Physics, School of Physical and Mathematical Sciences, Nanyang Technological University, Singapore 637371 Singapore;* orcid.org/0000-0003-3186-1041; Email: coldice@mail.ustc.edu.cn

Yue Lin − *Hefei National Laboratory for Physical Science at the Microscale, University of Science and Technology of China, Hefei 230026, Anhui, P. R. China;* orcid.org/0000-0001-5333-511X; Email: linyue@ustc.edu.cn

Authors

Mingling Li − *Hefei National Laboratory for Physical Science at the Microscale, University of Science and Technology of China, Hefei 230026, Anhui, P. R. China*

Mengyu Liu − *College of Physics and Energy, Fujian Normal University, Fuzhou 350117, P. R. China*

Yuhan Zhou − *College of Physics and Energy, Fujian Normal University, Fuzhou 350117, P. R. China*

Zhigao Huang − *College of Physics and Energy, Fujian Normal University, Fuzhou 350117, P. R. China; Fujian Provincial Key Laboratory of Quantum Manipulation and New Energy Materials, Fuzhou 350117, P. R. China; Fujian Provincial Collaborative Innovation Center for Optoelectronic Semiconductors and Efficient Devices, Xiamen 361005, P. R. China; Fujian Provincial Engineering Technology Research Center of Solar Energy Conversion and Energy Storage, Fuzhou 350117, China;* orcid.org/0000-0002-8157-3550

Fachun Lai − *College of Physics and Energy, Fujian Normal University, Fuzhou 350117, P. R. China; Fujian Provincial Key Laboratory of Quantum Manipulation and New Energy Materials, Fuzhou 350117, P. R. China; Fujian Provincial Collaborative Innovation Center for Optoelectronic Semiconductors and Efficient Devices, Xiamen 361005, P. R. China; Fujian Provincial Engineering Technology Research Center of Solar Energy Conversion and Energy Storage, Fuzhou 350117, China*

Complete contact information is available at: https://pubs.acs.org/10.1021/acsami.9b20142

Notes

The authors declare no competing financial interest.

■ ACKNOWLEDGMENTS

This work was financially supported by the Natural Science Foundation of China (nos. 11374052 and 11504359), the Natural Science Foundation of Fujian Province of China (2017 J05003), Education Department of Fujian Province (JA15140), and National Training Program of Innovation and Entrepreneurship for Undergraduates (201910394014). Dr. Lin acknowledges the supports from Youth Innovation Promotion Association of the Chinese Academy of Science (2020458), National Natural Science Foundation of China (11874334), joint funding supports from National Synchrotron Radiation Laboratory (KY2340000115), National Key Research and Development Program of China (2019YFA0307900) and Fundamental Research Funds for the Central Universities (Grant WK2060190103).

■ ABBREVIATIONS

1D, one-dimensional
PVD, physical vapor deposition

https://dx.doi.org/10.1021/acsami.9b20142
ACS Appl. Mater. Interfaces 2020, 12, 9909−9917

RTE, rapid thermal evaporation
VTD, vapor transport deposition
CSS, close-spaced sublimation
vdW, van der Waals
rPVD, rapid physical vapor deposition
FFT, fast Fourier transform
XRD, X-ray powder diffraction
SEM, scanning electron microscopy
AFM, atomic force microscopy
TEM, transmission electron microscopy
SAED, selected-area electron diffraction
EDX, energy-dispersive X-ray
HR-TEM, high-resolution TEM

REFERENCES

(1) Chen, H.; Liu, H.; Zhang, Z.; Hu, K.; Fang, X. Nanostructured Photodetectors: From Ultraviolet to Terahertz. *Adv. Mater.* **2016**, *28*, 403−433.
(2) Lu, J.; Liu, H.; Zhang, X.; Sow, C. H. One-dimensional nanostructures of II−VI ternary alloys: synthesis, optical properties, and applications. *Nanoscale* **2018**, *10*, 17456−17476.
(3) Wen, X.; Chen, C.; Lu, S.; Li, K.; Kondrotas, R.; Zhao, Y.; Chen, W.; Gao, L.; Wang, C.; Zhang, J.; Niu, G.; Tang, J. Vapor transport deposition of antimony selenide thin film solar cells with 7.6% efficiency. *Nat. Commun.* **2018**, *9*, 2179.
(4) Lu, X.; Khatib, O.; Du, X.; Duan, J.; Wei, W.; Liu, X.; Bechtel, H. A.; D'Apuzzo, F.; Yan, M.; Buyanin, A.; Fu, Q.; Chen, J.; Salmeron, M.; Zeng, J.; Raschke, M. B.; Jiang, P.; Bao, X. Nanoimaging of Electronic Heterogeneity in Bi_2Se_3 and Sb_2Te_3 Nanocrystals. *Adv. Electron. Mater.* **2018**, *4*, 1700377.
(5) Chen, C.; Bobela, D. C.; Yang, Y.; Lu, S.; Zeng, K.; Ge, C.; Yang, B.; Gao, L.; Zhao, Y.; Beard, M. C.; Tang, J. Characterization of basic physical properties of Sb_2Se_3 and its relevance for photovoltaics. *Front. Optoelectron.* **2017**, *10*, 18−30.
(6) Li, Z.; Liang, X.; Li, G.; Liu, H.; Zhang, H.; Guo, J.; Chen, J.; Shen, K.; San, X.; Yu, W.; Schropp, R. E. I.; Mai, Y. 9.2%-efficient core-shell structured antimony selenide nanorod array solar cells. *Nat. Commun.* **2019**, *10*, 125.
(7) Chen, G.; Wang, W.; Wang, C.; Ding, T.; Yang, Q. Controlled Synthesis of Ultrathin Sb_2Se_3 Nanowires and Application for Flexible Photodetectors. *Adv. Sci.* **2015**, *2*, 1500109.
(8) Kim, J.; Yang, W.; Oh, Y.; Lee, H.; Lee, S.; Shin, H.; Kim, J.; Moon, J. Self-oriented Sb_2Se_3 nanoneedle photocathodes for water splitting obtained by a simple spin-coating method. *J. Mater. Chem. A* **2017**, *5*, 2180−2187.
(9) Ma, J.; Wang, Y.; Wang, Y.; Peng, P.; Lian, J.; Duan, X.; Liu, Z.; Liu, X.; Chen, Q.; Kim, T.; Yao, G.; Zheng, W. One-dimensional Sb_2Se_3 nanostructures: solvothermal synthesis, growth mechanism, optical and electrochemical properties. *CrystEngComm* **2011**, *13*, 2369−2374.
(10) Yu, Y.; Wang, R. H.; Chen, Q.; Peng, L. M. High-Quality Ultralong Sb_2Se_3 and Sb_2S_3 Nanoribbons on a Large Scale via a Simple Chemical Route. *J. Phys. Chem. B* **2006**, *110*, 13415−13419.
(11) Song, H.; Li, T.; Zhang, J.; Zhou, Y.; Luo, J.; Chen, C.; Yang, B.; Ge, C.; Wu, Y.; Tang, J. Highly Anisotropic Sb_2Se_3 Nanosheets: Gentle Exfoliation from the Bulk Precursors Possessing 1D Crystal Structure. *Adv. Mater.* **2017**, *29*, 1700441.
(12) Liu, J.; Zhou, Y.; Liang, Y.; Liu, M.; Huang, Z.; Lin, L.; Zheng, W.; Lai, F. Large scale SnSe pyramid structure grown by gradient vapor deposition method. *CrystEngComm* **2018**, *20*, 1037−1041.
(13) Zhou, Y.; Wang, L.; Chen, S.; Qin, S.; Liu, X.; Chen, J.; Xue, D.-J.; Luo, M.; Cao, Y.; Cheng, Y.; Sargent, E. H.; Tang, J. Thin-film Sb_2Se_3 photovoltaics with oriented one-dimensional ribbons and benign grain boundaries. *Nat. Photonics* **2015**, *9*, 409.
(14) Chen, C.; Li, K.; Chen, S.; Wang, L.; Lu, S.; Liu, Y.; Li, D.; Song, H.; Tang, J. Efficiency Improvement of Sb_2Se_3 Solar Cells via Grain Boundary Inversion. *ACS Energy Lett.* **2018**, *3*, 2335−2341.
(15) Yuan, C.; Zhang, L.; Liu, W.; Zhu, C. Rapid thermal process to fabricate Sb_2Se_3 thin film for solar cell application. *Sol. Energy* **2016**, *137*, 256−260.
(16) Zhong, M.; Wang, X.; Liu, S.; Li, B.; Huang, L.; Cui, Y.; Li, J.; Wei, Z. High-performance photodetectors based on Sb_2S_3 nanowires: wavelength dependence and wide temperature range utilization. *Nanoscale* **2017**, *9*, 12364−12371.
(17) Ma, Z.; Chai, S.; Feng, Q.; Li, L.; Li, X.; Huang, L.; Liu, D.; Sun, J.; Jiang, R.; Zhai, T.; Xu, H. Chemical Vapor Deposition Growth of High Crystallinity Sb_2Se_3 Nanowire with Strong Anisotropy for Near-Infrared Photodetectors. *Small* **2019**, *15*, 1805307.
(18) Sun, G.; Li, B.; Li, J.; Zhang, Z.; Ma, H.; Chen, P.; Zhao, B.; Wu, R.; Dang, W.; Yang, X.; Tang, X.; Dai, C.; Huang, Z.; Liu, Y.; Duan, X.; Duan, X. Direct van der Waals epitaxial growth of 1D/2D Sb_2Se_3/WS_2 mixed-dimensional p-n heterojunctions. *Nano Res.* **2019**, *12*, 1139−1145.
(19) Liu, J.; Zhou, Y.; Lin, Y.; Li, M.; Cai, H.; Liang, Y.; Liu, M.; Huang, Z.; Lai, F.; Huang, F.; Zheng, W. Anisotropic Photoresponse of the Ultrathin GeSe Nanoplates Grown by Rapid Physical Vapor Deposition. *ACS Appl. Mater. Interfaces* **2019**, *11*, 4123−4130.
(20) Huang, L.; Gao, Q.; Sun, L.-D.; Dong, H.; Shi, S.; Cai, T.; Liao, Q.; Yan, C.-H. Composition-Graded Cesium Lead Halide Perovskite Nanowires with Tunable Dual-Color Lasing Performance. *Adv. Mater.* **2018**, *30*, 1800596.
(21) Gutiérrez, H. R.; Perea-López, N.; Elías, A. L.; Berkdemir, A.; Wang, B.; Lv, R.; López-Urías, F.; Crespi, V. H.; Terrones, H.; Terrones, M. Extraordinary Room-Temperature Photoluminescence in Triangular WS_2 Monolayers. *Nano Lett.* **2013**, *13*, 3447−3454.
(22) Molina-Sánchez, A.; Wirtz, L. Phonons in single-layer and few-layer MoS_2 and WS_2. *Phys. Rev. B* **2011**, *84*, 155413.
(23) Matolínová, I.; Gillet, M.; Gillet, E.; Matolín, V. A study of tungsten oxide nanowires self-organized on mica support. *Nanotechnology* **2009**, *20*, 445604.
(24) Röthel, C.; Radziown, M.; Resel, R.; Zimmer, A.; Simbrunner, C.; Werzer, O. Complex Behavior of Caffeine Crystallites on Muscovite Mica Surfaces. *Cryst. Growth Des.* **2015**, *15*, 4563−4570.
(25) Wang, Y.; Shi, Y.; Xin, G.; Lian, J.; Shi, J. Two-Dimensional van der Waals Epitaxy Kinetics in a Three-Dimensional Perovskite Halide. *Cryst. Growth Des.* **2015**, *15*, 4741−4749.
(26) Koma, A. Van der Waals epitaxy for highly lattice-mismatched systems. *J. Cryst. Growth* **1999**, *201-202*, 236−241.
(27) Lee, H. N.; Hesse, D.; Zakharov, N.; Gösele, U. Ferroelectric $Bi_{3.25}La_{0.75}Ti_3O_{12}$ Films of Uniform a-Axis Orientation on Silicon Substrates. *Science* **2002**, *296*, 2006−2009.
(28) Chen, J.; Fu, Y.; Samad, L.; Dang, L.; Zhao, Y.; Shen, S.; Guo, L.; Jin, S. Vapor-Phase Epitaxial Growth of Aligned Nanowire Networks of Cesium Lead Halide Perovskites ($CsPbX_3$, X = Cl, Br, I). *Nano Lett.* **2017**, *17*, 460−466.
(29) Cheng, R.; Wen, Y.; Yin, L.; Wang, F.; Wang, F.; Liu, K.; Shifa, T. A.; Li, J.; Jiang, C.; Wang, Z.; He, J. Ultrathin Single-Crystalline CdTe Nanosheets Realized via Van der Waals Epitaxy. *Adv. Mater.* **2017**, *29*, 1703122.
(30) Island, J. O.; Biele, R.; Barawi, M.; Clamagirand, J. M.; Ares, J. R.; Sánchez, C.; van der Zant, H. S. J.; Ferrer, I. J.; D'Agosta, R.; Castellanos-Gomez, A. Titanium trisulfide (TiS3): a 2D semiconductor with quasi-1D optical and electronic properties. *Sci. Rep.* **2016**, *6*, 22214.
(31) Lu, W.; Ma, X.; Fei, Z.; Zhou, J.; Zhang, Z.; Jin, C.; Zhang, Z. Probing the anisotropic behaviors of black phosphorus by transmission electron microscopy, angular-dependent Raman spectra, and electronic transport measurements. *Appl. Phys. Lett.* **2015**, *107*, No. 021906.
(32) Zhou, X.; Hu, X.; Jin, B.; Yu, J.; Liu, K.; Li, H.; Zhai, T. Highly Anisotropic GeSe Nanosheets for Phototransistors with Ultrahigh Photoresponsivity. *Adv. Sci.* **2018**, *5*, 1800478.
(33) Li, L.; Wang, W.; Gong, P.; Zhu, X.; Deng, B.; Shi, X.; Gao, G.; Li, H.; Zhai, T. 2D GeP: An Unexploited Low-Symmetry Semiconductor with Strong In-Plane Anisotropy. *Adv. Mater.* **2018**, *30*, 1706771.

https://dx.doi.org/10.1021/acsami.9b20142
ACS Appl. Mater. Interfaces 2020, 12, 9909−9917

(34) Li, M.; Wu, Y.; Li, T.; Chen, Y.; Ding, H.; Lin, Y.; Pan, N.; Wang, X. Revealing anisotropy and thickness dependence of Raman spectra for SnS flakes. *RSC Adv.* **2017**, *7*, 48759−48765.

https://dx.doi.org/10.1021/acsami.9b20142
ACS Appl. Mater. Interfaces 2020, 12, 9909−9917